ACS Nano, 2015, 9 (10), pp 10237–10243. DOI: 10.1021/acsnano.5b03980

Atomic-scale Magnetism of Cr-doped Bi_2Se_3 Thin Film Topological Insulators

Wenqing Liu,[1,2,†] Damien West,[3,†] Liang He,[1,4,†] Yongbing Xu,[1,2,] Jun Liu,[5] Kejie Wang,[1] Yong Wang,[5] Gerrit van der Laan,[6] Rong Zhang[1,*] Shengbai Zhang[3,*] Kang. L. Wang,[4,*]*

[1] York-Nanjing Joint Center (YNJC) for spintronics and nanoengineering, School of Electronics Science and Engineering, Nanjing University, Nanjing, 210093, China

[2] Spintronics and Nanodevice Laboratory, Department of Electronics, University of York, York YO10 5DD, UK

[3] Department of Physics, Applied Physics, and Astronomy, Rensselaer Polytechnic Institute, Troy, New York 12180, USA

[4] Department of Electrical Engineering, University of California, Los Angeles, Los Angeles, CA 9009, USA

[5] Center of Electron Microscopy, State Key Laboratory of Silicon Materials, Department of Materials Science and Engineering, Zhejiang University, Hangzhou, 310027, China

[6] Magnetic Spectroscopy Group, Diamond Light Source, Didcot OX11 0DE, UK

[†] Authors contributed equally to this work.

*Authors to whom correspondence should be addressed. Electronic addresses: yongbing.xu@york.ac.uk, rzhang@nju.edu.cn, zhangs9@rpi.edu, and wang@seas.ucla.edu

Abstract: Magnetic doping is the most common method for breaking time-reversal-symmetry surface states of topological insulators (TIs) to realize novel physical phenomena and to create beneficial technological applications. Here we present a study of the magnetic coupling of a prototype magnetic TI, i.e., Cr-doped Bi_2Se_3, in its ultrathin limit which is expected to give rise to quantum anomalous Hall (QAH) effect. The high quality $Bi_{2-x}Cr_xSe_3$ epitaxial thin film was prepared using molecular beam epitaxy (MBE), characterized with scanning transimission electron microscope (STEM), electrical magnetotransport, and x-ray magnetic circularly dichroism (XMCD) techniques and the results were simulated using density functional theory (DFT) with spin-orbit coupling (SOC). We observed a sizable spin moment m_{spin} = (2.05 ± 0.20) μ_B/Cr and a small and negative orbital moment m_{orb} = (-0.05 ± 0.02) μ_B/Cr of the $Bi_{1.94}Cr_{0.06}Se_3$ thin film at 2.5 K. A remarkable fraction of the $(Cr_{Bi}\text{-}Cr_I)^{3+}$ antiferromagnetic dimer in the $Bi_{2-x}Cr_xSe_3$ for $0.02 < x < 0.40$ was obtained using *first-principles* simulations , which was neglected in previous studies. The spontaneous coexistence of ferro- and antiferromagnetic Cr defects in $Bi_{2-x}Cr_xSe_3$ explains our experimental observations and those based on conventional magnetometry which universally report magnetic moments significantly lower than 3 μ_B/Cr predicted by Hund's rule.

Keywords: *Magnetic topological insulator*, spin and orbital moments, XMCD, density functional theory, and spintronics.

Three-dimensional topological insulators (TIs) represent unusual phases of quantum matter with an insulating bulk gap and gapless Dirac-like band dispersion surface states. Unlike the different electronic properties of the surface and the bulk universally existing in all solids owing to the inevitable termination of the periodic lattice structure near the surface, TIs present a new class of nontrivial surface states arising from the intrinsic strong SOC. These robust low-dimensional conducting states are topologically protected against time-reversal-invariant perturbations, such as scattering by non-magnetic impurities, crystalline defects, and surface distortions. While such a phase offers unique opportunities for fundamental research, it is equally important to break the time-reversal symmetry of TIs to realize novel physical phenomena and quantum-computing applications. The newly demonstrated QAH effect,[1,2,3] abnormal proximity effect,[4,5] giant magneto-optical Kerr effect,[6] magnetic monopole,[7] and chiral conduction channels[8,9] are some of the fascinating examples. Within the growing family of TIs, ferromagnetism has been reported in V-, Cr-, and Mn-doped single crystals of Sb_2Te_3,[10,11] Fe- and Mn-doped single crystals of Bi_2Te_3,[12,13] and Mn-doped single crystals of Bi_2Se_3.[14] Both ferro-[15] and antiferro-magnetism[16] have been reported in Cr-doped Bi_2Se_3, and for Fe-doped Bi_2Se_3 observations are rather controversial. Zhang *et al*.[17] studied the effect of magnetic doping of a series of 3*d* transition metals in Bi_2Se_3 using *first-principles* calculations and found that Cr and Fe doping preserves the insulating nature of the host TI in the bulk and Cr-doped Bi_2Se_3 is likely to be ferromagnetic. Apart from transition metals, rare-earth metals such as Gd[18], Dy, and Sm[19] have also been explored as an effective dopant to induce long-range magnetic ordering in Bi_2Se_3[20] or Bi_2Te_3.

For the electronic and magnetic ground state of the magnetically doped TIs, evidence from the experimental observations including magneto-transport measurements,[51,52] global magnetometry,[14,15,51] and core-level spectroscopies[21,22,23] are so far inconclusive. Magnetic studies on epitaxial, Cr-doped Bi_2Se_3 using superconducting quantum interference device - vibrating sample magnetometer magnetometry (SQUID-VSM)[15] and polarized neutron reflectometry (PNR)[24] universally reported a magnetic moment of no more than ~2 μ_B/atom, remarkably lower than the Hund's rule of 3 μ_B/atom of substitutional Cr^{3+} on Bi sites. Significant mismatch also exists in Mn- and Fe-doped Bi_2Se_3, who typically show global magnetic moments of ~1.5 μ_B/atom and ~3μ_B/atom,[14] while their Hund's rule is 5 μ_B/atom. Table 1 gathers the magnetic moment of Bi_2Se_3 for various magnetic dopants. It has been proposed that in magnetic TIs, ferromagnetic moments can be developed not only through the *s-d* exchange interaction such as in diluted magnetic semiconductors (DMSs),[25,26,27,28,29] but also through the van Vleck

mechanism, by which magnetic ions are directly coupled through the local valance elecrons.[3] Both types of mechanism have been observed independently in Mn-doped $Bi_2(TeSe)_3$[30] and Cr-doped $(BiSb)_2Te_3$[31] thin films. Given the fact that the magnetic state of a doped TI can be independent of the carrier concentration, it is timely and important to obtain an insight of the detailed chemical bonds of the magnetic impurities. In this regard, the synchrotron-based techniques of XMCD are ideal valence-, site-, and symmetry-specific probes.[32, 23, 33, 34, 35, 36, 37] In this Letter, we present a comprehensive study of magnetism of a prototypical magnetic TI, i.e., $Bi_{2-x}Cr_xSe_3$, in its ultrathin limit which is expected to give rise to QAH effect.[3] According to the pioneering work by Haazen *et al*.,[15] the magnetic moment of $Bi_{2-x}Cr_xSe_3$ decreases with increasing doping concentration and sharply drops beyond ~10%. On the other hand, excessively low Cr concentrations, i.e., < 1%, form no long-range magnetic ordering.[51] Therefore, we selected a 3% Cr-doped Bi_2Se_3 or $Bi_{1.94}Cr_{0.06}Se_3$ thin film to perform the detailed XMCD study. Using XAS and XMCD, we quantitatively addressed the magnetic moments of the epitaxial $Bi_{1.94}Cr_{0.06}Se_3$ thin film, and the results were compared with *first-principle* calculations to get an insight of the nature of the magnetic coupling.

Results and discussions

The 10-nm $Bi_{1.94}Cr_{0.06}Se_3$/Si(111) thin films used in this study was prepared using MBE. Firstly the crystalline structure of the prepared samples was characterized using high-angle annular dark-field (HAADF) high-resolution STEM. Cross-sectional foils of $Bi_{1.94}Cr_{0.06}Se_3$/Si(111) were prepared by focused ion beam (FIB), during which all parameters were carefully optimized to avoid ion injection and specimen damage, including the accelerating voltage, beam current, and tilt angle.[4] Figure 1a presents a typical HAADF image of the $Bi_{1.94}Cr_{0.06}Se_3$/Si(111), in which the Bi and Se columns (marked by red and blue solid circles, respectively) can be clearly identified owing to the *Z*-contrast sensitivity of the HAADF imaging technique. The dark regions outside $Bi_{1.94}Cr_{0.06}Se_3$ corresponds to the Al_2O_3 cap and Si substrate, respectively, which cannot be demonstrated using the present mode since they are composed of much lighter atoms than Bi and Se. The Cr dopants are uniformly distributed within the Bi_2Se_3 film, as can be seen from the EDX color maps of the Cr, Bi, and Se, respectively, in Figure 1b-d. Overall, the HAADF images confirm the highly ordered hexagonal and quintuple-layered structure of the prepared $Bi_{1.94}Cr_{0.06}Se_3$/Si(111) thin films without appreciable Cr segregations or secondary phases.[38, 39] It should be noted that even though these images solely are not sufficient to evidence the entry

modes of the Cr dopants in the Bi_2Se_3 matrix for the similar reason as the inaccessibility of the Al atoms.

The global magnetic response of the epitaxial $Bi_{1.96}Cr_{0.06}Se_3$/Si(111) thin film samples was examined by magneto-transport measurements by patterning into standard Hall bar devices, using conventional optical photolithography and a subsequent CHF_3 dry etching for 20 s. As shown in Figure 2a, six Hall channel contacts (10 nm Ti and 100 nm Au) were defined by e-beam evaporation. Standard four-terminal electrodes were fabricated to eliminate the contact resistance. A constant AC current of 0.05-0.1 μA with a frequency of 1.3 kHz is fed through two outer contacts, and the voltage drop across the inner pads is measured to determine the resistance. By subtracting the ordinary Hall component, we plotted the anomalous Hall resistance ($R_{AHE} = R_{xy} - R_0 \cdot H$)[40] as a function of the field applied perpendicularly to the film in Figure 2c, in which a non-zero R_{AHE} was observable up to ~30 K. Figure 2b presents the temperature dependence of the coercive field (H_c) estimated from the shift of the weak anti-localization (WAL) cusp under the opposite field scanning directions.[4, 51] The H_c exhibits Curie-like behavior against the temperature and $T_c \approx 30$ K, consistent with that estimated from R_{AHE}.

X-ray absorption spectroscopy (XAS) measurements at the Cr $L_{2,3}$ absorption edge of the $Bi_{1.96}Cr_{0.06}Se_3$/Si(111) thin film were performed on beamline I10 at the Diamond Light Source, UK. Circularly polarized x-rays with ~100% degree of polarization[41] were used in normal incidence with respect to the sample plane and parallel to the applied magnetic field, as illustrated in Figure 3a. The XMCD was obtained by taking the difference of the XAS spectra, i.e., $\sigma^- - \sigma^+$, by flipping the x-ray helicity at a fixed magnetic field of 30 kOe, under which the sample is fully magnetized with negligible paramagnetic contribution.[4, 51, 52] Figure 3b presents a typical pair of XAS and XMCD spectra of the $Bi_{1.96}Cr_{0.06}Se_3$/Si(111) epitaxial thin film obtained at 2.5 K using total electron yield detection (TEY). The XAS of Cr shows multiple structures for both spin-orbit split core levels, suggesting a mixture of Cr with more than one valence state. This mixture can be analyzed using atomic multiplet simulation of the spectrum as detailed in the supplementary materials, which indicates that the Cr dopants are primarily near-trivalent and the presence of a small amount of divalent Cr is most likely from the terminated surface of the $Bi_{2-x}Cr_xSe_3$ lattice.[21, 22]

The spin (m_{spin}) and orbital (m_{orb}) magnetic moment of the $Bi_{1.96}Cr_{0.06}Se_3$/Si(111) thin film were obtained by applying the sum rules[42, 43] to the integrated XMCD and summed XAS spectra of the Cr $L_{2,3}$ edges, based on

$$m_l = -\frac{4}{3} n_h \frac{\int_{L_{2,3}} (\sigma^- - \sigma^+)\, dE}{\int_{L_{2,3}} (\sigma^- + \sigma^+)\, dE}$$
$$m_s = -n_h \frac{6\int_{L_3} (\sigma^- - \sigma^+)\, dE - 4\int_{L_{2,3}} (\sigma^- - \sigma^+)\, dE}{\int_{L_{2,3}} (\sigma^- + \sigma^+)\, dE} \times SC - \langle T_z \rangle \quad (1)$$

where E, n_h, SC and $\langle T_z \rangle$, represent the photon energy, number of d holes, spin correction (SC) factor, and magnetic dipole term, respectively. In order to exclude the non-magnetic contribution of the XAS spectra an arctangent-based step function is used to fit the threshold.[44, 45] The spectral overlap or j-j mixing[42] has to be taken into account because of the relatively small spin-orbit splitting in the Cr 2p level. The value of SC, i.e., 2.0±0.2 for Cr, was determined by calculating the $L_{2,3}$ multiplet structure for a given ground state, applying the sum rule on the calculated XMCD spectrum, and comparing the result with the spin moment calculated directly for this ground state.[5, 46] Assuming $n_h = 7$ on the majority trivalent Cr basis (see supplementary materials), we obtained m_{spin} = (2.05 ± 0.20) μ_B/atom and m_{orb} = (-0.05 ± 0.02) for the $Bi_{1.94}Cr_{0.06}Se_3$/Si(111) thin film. That gives a total moment (m_{total}) of (2.00 ± 0.20) μ_B/atom as included in table 1. The m_{orb} and m_{spin} have opposite signs, corresponding to an antiparallel alignment of spin and orbital moments in Cr. This agrees with the Hund's rule for Cr where the 3d shell is less than half full. The octahedral crystal-field interaction quenches m_{orb}, because the 3d electrons occupy the three-fold degenerate majority-spin t_{2g} orbitals, leading to a nearly vanishing m_{orb} as observed here. For similar reasons the $\langle T_z \rangle$ is small and is not taken out from the m_{spin}, giving an error < 5%.

We address the origin of the observed m_{spin} and m_{orb} of the $Bi_{1.94}Cr_{0.06}Se_3$/Si(111) thin film to this end. The layered structure of Bi_2Se_3 allows the Cr dopants not only to enter the host substitutionally, but also interstitially in the van der Waals gap between the layers. To investigate the m_{spin} and m_{orb} of Cr in Bi_2Se_3, it must first be determined where the Cr prefers to reside within the lattice. Although several prior works[47] have reported that substitutional Cr is energetically more favorable over interstitial Cr, if one considers only single impurities, these calculations leave out the possibility of the presence of complex defects. We calculated the formation energies (ΔH) of Cr at various lattice positions including not only the interstitial (denoted as Cr_I) and substitutional sites with Cr replacing Bi (denoted as Cr_{Bi}) and Se (denoted as Cr_{Se}), but also the large defect complexes containing pairs of Cr-atoms, such as the Cr_{Bi}-Cr_{Se} and Cr_{Bi}-Cr_I. As illustrated in Figure 4b, the predominant defects in the system were found to be Cr_I^{3+}, Cr_{Bi}^{0}, and $(Cr_{Bi}\text{-}Cr_I)^{3+}$ complex whose calculated ΔH, excluding SOC, for Fermi energies (E_F) ranging from

the valance band maximum (VBM) to the conduction band minimum (CBM) are presented in Figure 4a. We ruled out the possibilities of Cr_{Se} and Cr_{Se}-Cr_{Bi} as the ΔH of them was found to be high (> 1 eV). Table 2 presents the ΔH and the magnetic moments of the three low-energy defects, namely, Cr_I, Cr_{Bi}, and Cr_{Bi}-Cr_I caculated including SOC. While both Cr_{Bi} and Cr_I have m_{spin} of ~3 μ_B/atom, the Cr_{Bi}-Cr_I pair is antiferromagnetic (with the high-spin magnetic configuration 75 meV higher in energy) with a nearly vanished m_{spin}. In consistent with the XMCD-derived m_{orb}, the calculation also gives small and negative m_{orb} for the Cr dopants due to the effect of the crystal field. This indicates that Cr retains its small SOC nature, even when incoopertaed into a strong SOC system like Bi_2Se_3.

Figure 5 presents the dependence of the Cr content, average magnetic moment, and the relative concentrations, respectively, of the most common Cr related defects as a function of the chemical potential of Cr with the E_F pinned at the CBM. While the antiferromagnetic Cr_{Bi}-Cr_I pair is the dominant defect for large Cr concentrations, as the Cr chemical potential decreases (and hence the amount of incorporated Cr), entropy works against the pair formation, and Cr_{Bi} becomes the dominant defect. This can be seen in Figure 5b, which shows the relative probabilities of the different defects as a function of $_{Cr}$ which was calculated by minimizing the free energy of the system with respect to the number of defects (see supplementary materials). It should be noted that the position of the crossover between the stability of the Cr_{Bi} and Cr_{Bi}-Cr_I defects, depicted in Figure 5b, depends on the $_{Bi}$. As we tend toward Se-rich growth conditions, Cr_{Bi} becomes the dominant defect for all Cr concentrations. We treated the $_{Bi}$ as a fitting parameter and find that the observed data for m_{spin} can be best described when $_{Bi} \approx 150$ meV below $_{Bi}^{bulk}$. This proximity to the Bi-rich condition is well observed in MBE grown samples which typically have high Se vacancy concentrations, despite their high Se deposition rates.[51, 52] The dependence of the average magnetic moment per Cr is shown in Figure 5a. The change in stability between Cr_{Bi} and the Cr_{Bi}-Cr_I pair leads to an average magnetic moment which explictly depends on the Cr chemical potential. In agreement with the ponieering reports by Zhang *et al.*,[48, 49] we found that Bi substitutional sites are more stable than interstitial sites for Cr impurities. However, the Cr_{Bi}-Cr_I bonding can significantly alter ΔH, leaving the $(Cr_{Bi}$-$Cr_I)^{3+}$ complex even lower in energy than either Cr_{Bi} or Cr_I for high Cr doping concentrations. The spontaneous coexistence of ferro- and antiferromagnetic Cr in $Bi_{2-x}Cr_xSe_3$ explains not only the experimental results of our work based on XMCD, but also observations such as by Haazen *et al.*[50] using SQUID-VSM and by Collins-McIntyre *et al.*[24] using PNR, who both reported mismatches between the observed magnetic moment of $Bi_{2-x}Cr_xSe_3$ and the Hund's rule value of 3 μ_B/atom for

substitutional Cr^{3+} on Bi sites. In consistent with the pioneering experimental reports,[5,51,52,53] we found that the growth temperature varying between 200 and 300 °C results in no significant difference of the type and distribution the Cr-related defects while below 200 °C, more antiferromagnetic Cr defects can presence.

Conclusions

To summarize, we have presented a comprehensive study of the Cr m_{spin} and m_{orb} of a prototype magnetic TI, i.e., $Bi_{2-x}Cr_xSe_3$, in the ultrathin limit which is expected to give rise to QAH effect. The high quality $Bi_{1.94}Cr_{0.06}Se_3$/Si(111) epitaxial thin film was prepared using MBE, carefully characterized with STEM, magnetotransport and XMCD measurements. We have quantitatively addressed the m_{spin} and m_{orb} of the $Bi_{2-x}Cr_xSe_3$/Si(111) thin films and the results agree well with DFT caculations. The XMCD-derived m_{spin} is remarkably lower than Hund's rule value and the m_{orb} is negative and largely quecnhed. We obtained a remarkable fraction of the $(Cr_{Bi}\text{-}Cr_I)^{3+}$ antiferromagnetic dimers in $Bi_{2-x}Cr_xSe_3$ for $0.02 < x < 0.40$, which has been neglected in previously reported studies. The spontaneous coexistence of ferro- and antiferro-magnetic Cr defects in $Bi_{2-x}Cr_xSe_3$ explains the experimental observations of this work as well as those based on conventional magnetometry that universally report magnetic moments significantly lower than that predicted by the Hund's rule. Our work provides direct evidence for the detailed magnetic states of the magnetically doped TIs in thin film form. Future work to explore the tuning of the magnetization of TIs and its dependence on the band filling will have strong implications for both fundamental physics and emerging spintronics technology.

Methods

Sample preparations. The 10-nm $Bi_{2-x}Cr_xSe_3$ thin films used in this study were grown in ultra-high vacuum (UHV) using a Perkin-Elmer MBE system on Si(111) substrates using the well-established recipe.[51,52,53] High-purity Bi (99.9999%) was evaporated from conventional effusion cells at 470 °C, while Se (99.99%) was created from a cracker cell (SVTA) at 240 °C. The substrates were pre-annealed at 200°C in UHV until the two-dimensional streak pattern appeared as monitored by the real-time reflection high-energy electron diffraction (RHEED). The desired doping concentrations of Cr were obtained by evaporating Cr (99.99%) from the effusion cell at different temperatures and calibrated by energy dispersive x-ray analysis. Immediately after the

growth of the $Bi_{1.94}Cr_{0.06}Se_3$ thin film, 2-nm Al was *in-situ* evaporated onto the sample to protect it from oxidation and environmental doping during transport to the synchrotron facility.

ΔH Calculations. The *first-principles* DFT calculations were performed within the Perdew-Burke-Ernzerhof (PBE) generalized gradient approximation (GGA).[54] The Bi (5*d,* 6*s,* 6*p*), Se (4*s,* 4*p*), and Cr (3*p,* 3*d,* 4*s*) orbitals are explicitly treated in the valence and interactions between the ion cores and valence electrons are described by the projector augmented wave (PAW)[55,56] method as implemented in the VASP code.[57, 58] Since SOC has shown to be important to describe the defect properties of Bi_2Se_3,[59] the magnetic properties and formation energies of the low energy defects were also calculated with SOC implemented in the all-electron part of the PAW Hamiltonian within the muffin-tin spheres. The basis set consisted of plane waves with a kinetic energy cutoff of 270 eV and the total energy was calculated with a Brillouin zone sampling of 2 × 2 × 2.[60] Structural relaxations of the defects were performed in a 4 × 4 supercell containing 3 quintuple layers (QLs) with 95 Bi and 145 Se atoms and proceeded until the largest Hellmann-Feynman force was less than 0.025 eV/A. The ΔH of the defects were calculated in the low-density limit according to

$$\Delta H = E(D^q) - E_{bulk} + \sum_i \Delta n_i \mu_i + q(E_F + E_{VBM}) \qquad (2)$$

where $E(D^q)$, E_{bulk}, μ_i, Δn_i, respectively, represent the energy of the supercell containing the defect in charge state q, the energy of the defect-free bulk supercell, the chemical potential of the i^{th} atomic species, and the number of those which has changed in the formation of the defect.[61]

Conflict of Interest

The authors declare no competing financial interest.

Acknowledgement

This work is supported by the State Key Program for Basic Research of China (Grants No. 2014CB921101, 2013CB934600 and 2011CB921404), NSFC (Grants No. 61274102, 61474061 21473168, 11174244, 51390474, and 11234011), Zhejiang Provincial Natural Science Foundation of China (LR12A04002), the Ministry of Education (20120101110087, IRT13037),

and UK STFC. Diamond Light Source is acknowledged for beamtime on I10. D.W. acknowledges support of the Defense Award Research Project Agency (DARPA), Award No. N66001-12-1-4304, and S.B.Z. acknowledges support of the US Department of Energy (DOE) under Grant No. DE-SC0002623. Supercomputer time was provided by NERSC under the Grant No. DE-AC02-05CH11231 and the Center for Computational Innovations (CCI) at Rensselaer Polytechnic Institute.

Associated content

Supplementary materials accompany this paper.

TABLES

System	Method	m_{total} (μ_B/atom)	Ref
$Bi_{1.94}Cr_{0.06}Se_3$	XMCD	2.00 ± 0.20	†
$Bi_{1.98}Cr_{0.02}Se_3$	SQUID-VSM	0.4	18
$Bi_{1.76}Cr_{0.24}Se_3$	Neutron scattering	1.5	24
$Bi_{1.90}Cr_{0.1}Se_3$	SQUID-VSM	2.0	15
$Bi_{1.77}Cr_{0.23}Se_3$	XMCD	2.9 ± 0.3	21
$Bi_{1.98}Mn_{0.02}Se_3$	SQUID-VSM	1.5	14
$Bi_{1.995}Fe_{0.005}Se_3$	SQUID-VSM	3.2	14
$Bi_{1.98}Gd_{0.02}Se_3$	SQUID-VSM	6.9 ± 0.2	18

Table 1. Reported experimental values for the magnetic moment of magnetically doped Bi_2Se_3. † refers to this work.

Cr defect	Method	ΔH (eV)	m_{spin} (μ_B/atom)	m_{orb} (μ_B/atom)	m_{total} (μ_B/atom)
3%	XMCD		2.05 ± 0.20	-0.05 ± 0.02	2.00 ± 0.20
3%	PBE		1.90	-0.03	1.87
Cr_I^{3+}	PBE	-0.03	2.98	-0.03	2.95
Cr_{Bi}^{0}	PBE	-0.21	2.93	-0.02	2.91
$(Cr_I\text{-}Cr_{Bi})^{3+}$	PBE	-0.68	0.01	-0.04	-0.03

Table 2. Calculated magnetic moments of the low-energy Cr related defects in Bi_2Se_3 and that derived from XMCD measurements as described in the text. The calculated results include SOC and correspond to the E_F at the CBM with μ_{Cr} and μ_{Bi} equal to their respective bulk values.

References

[1] Chang, C.-Z. et al. *Science* **2013**, *340*, 167–170.

[2] Liu, C.-X.; Qi, X.-L.; Dai, X.; Fang, Z.; Zhang, S.-C. *Phys. Rev. Lett.* **2008**, *101*, 146802.

[3] Yu, R.; Zhang, W.; Zhang, H.-J.; Zhang, S.-C.; Dai, X.; Fang, Z. *Science* **2010**, *329*, 61–64.

[4] Qin, W.; Zhang, Z. *Phys. Rev. Lett.* **2014**, *113*, 266806.

[5] Liu, W. et al. *Nano Lett.* **2015**, *15*, 764–769.

[6] Tse, W.-K.; MacDonald, A. H. *Phys. Rev. Lett.* **2010**, *105*, 057401.

[7] Qi, X.; Li, R.; Zang, J.; Zhang, S. *Science* **2009**, *323*, 1184–1187.

[8] Qi, X.-L.; Hughes, T. L.; Zhang, S.-C. *Phys. Rev. B* **2008**, *78*, 195424.

[9] Tserkovnyak, Y.; Loss, D. *Phys. Rev. Lett.* **2012**, *108*, 187201.

[10] Dyck, J.; Hájek, P.; Lošt'ák, P.; Uher, C. *Phys. Rev. B* **2002**, *65*, 115212.

[11] Dyck, J.; Drašar, Č.; Lošt'ák, P.; Uher, C. *Phys. Rev. B* **2005**, *71*, 115214.

[12] Hor, Y. S. et al. *Phys. Rev. B* **2010**, *81*, 195203.

[13] Kulbachinskii, V.A. et al. *Phys. B Condens. Matter* **2002**, *311*, 292–297.

[14] Chen, Y. L. et al. *Science* **2010**, *329*, 659–662.

[15] Haazen, P. P. J. et al. *Appl. Phys. Lett.* **2012**, *100*, 082404.

[16] Choi, Y. H. et al. *J. Appl. Phys.* **2011**, *109*, 07E312.

[17] Zhang, J.-M.; Zhu, W.; Zhang, Y.; Xiao, D.; Yao, Y. *Phys. Rev. Lett.* **2012**, *109*, 266405.

[18] Song, Y. R. et al. *Appl. Phys. Lett.* **2012**, *100*, 242403.

[19] Chen, T. et al. *Adv. Mat.* **2015**, DOI: 10.1002/adma.201501254.

[20] Harrison, S. E. et al. *J. Phys. Condens. Matter* **2015**, *27*, 245602.

[21] Figueroa, A. I. et al. *Phys. Rev. B* **2014**, *90*, 134402.

[22] Collins-McIntyre, L. J. et al. *AIP Adv.* **2014**, *4*, 127136.

[23] Watson, M. D. et al. *New J. Phys.* **2013**, *15*, 103016.

[24] Collins-McIntyre, L. J. et al. *Europhysics Lett.* **2014**, *107*, 57009.

[25] Edmonds, K. W. et al. *Phys. Rev. Lett.* **2011**, *107*, 197601.

[26] Ruderman, M. A. & Kittel, C. *Phys. Rev.* **1954**, *96*, 99–102.

[27] Yosida, K. *Phys. Rev.* **1957**, 106, 893–898

[28] Jungwirth, T.; Sinova, J.; Masek, J.; Kucera, J.; MacDonald, A. H. Rev. *Mod. Phys.* **2006**, *78*, 809–864.

[29] Hong, N. H.; Sakai, J.; Poirot, N.; Brizé, V. *Phys. Rev. B* **2006**, *73*, 132404.

[30] Checkelsky, J. G.; Ye, J.; Onose, Y.; Iwasa, Y.; Tokura, Y. *Nat. Phys.* **2012**, *8*, 729–733.

[31] Chang, C.-Z. et al. *Adv. Mater.* **2013**, *25*, 1065–1070.

[32] Tjeng, L. H.; Idzerda, Y. U.; Rudolf, P.; Sette, F.; Chen, C. T. *J. Magn. Magn. Mater.* **1992**, *109*, 288–292.

[33] Kronast, F. et al. *Phys. Rev. B* **2006**, *74*, 235213.

[34] Liu, W.Q. et al. *Sci. Rep.* **2015**, *5*, 11911.

[35] Vobornik, I. et al. *Nano Lett.* **2011**, *11*, 4079–4082.

[36] Li, J. et al. *Phys. Rev. B* **2012**, *86*, 054430.

[37] Tserkovnyak, Y.; Pesin, D. A.; Loss, D. *Phys. Rev. B* **2015**, *91*, 041121(R).

[38] Clarke, S. M.; Freedman, D. E. *Inorg. Chem.* **2015**, *22*, 2765.

[39] Ji, H.; Allred, J. M.; Ni, N.; Tao, J.; Neupane, M.; Wray, a.; Xu, S.; Hasan, M. Z.; Cava, R. J. *Phys. Rev. B* **2012**, *85*, 165313.

[40] Nagaosa, N.; Sinova, J.; Onoda, S.; MacDonald, A. H.; Ong, N. P. *Rev. Mod. Phys.* **2010**, *82*, 1539–1592.

[41] Wang, H.; Bencok, P.; Steadman, P.; Longhi, E.; Zhu, J.; Wang, Z. *J. Synchrotron Radiat.* **2012**, *19*, 944–948.

[42] Thole, B. T.; Carra, P., Sette, F., and van der Laan, G., *Phys. Rev. Lett.* **1992**, *68*, 1943.

[43] Carra, P.; Thole, B.T. Altarelli, M., Wang, X. *Phys. Rev. Lett.* **1993**, *70*, 694.

[44] Liu, W. Q. et al. *Appl. Phys. Lett.* **2014**, *104*, 142407.

[45] Liu, W. Q. et al. *J. Appl. Phys.* **2015**, *117*, 17E121.

[46] van der Laan, G.; Thole, B. T. *Phys. Rev. B* **1991**, *43*, 13401.

[47] Zhang, J.-M.; Zhu, W.; Zhang, Y.; Xiao, D.; Yao, Y. *Phys. Rev. Lett.* **2012**, *109*, 266405.

[48] Zhang, J.-M. et al. *Phys. Rev. Lett.* **2012**, 109**,** 266405.

[49] Zhang, J.-M. et al. *Phys. Rev. B* **2013**, *88*, 235131.

[50] Zhang, D. et al. *Phys. Rev. B* **2012**, *86*, 205127.

[51] Kou, X. F. et al. *J. Appl. Phys.* **2012**, *112*, 063912.

[52] Kou, X. F. et al. *Nano Lett.* **2013**, *13*, 4587–4593.

[53] Kou, X.; Lang, M.; Fan, Y.; Jiang, Y.; Nie, T. *ACS Nano* **2013**, 9205–9212.

[54] Perdew, J.P.; Burke, K.; Ernzerhof, M. *Phys. Rev. Lett.* **1996,** 77, 3865.

[55] Blochl, P.E. *Phys. Rev. B* **1994**, 50, 17953.

[56] Kresse, G.; Joubert, D. *Phys. Rev. B* **1999**, 59, 1758.

[57] Kresse, G.; Hafner, J. *Phys. Rev. B* **1993**, 47, 558.

[58] Kresse, G.; Furthmuller, J. *Phys. Rev. B* **1996**, 54, 11169.

[59] West, D.; Sun, Y.Y.; Wang, H.; Bang, J.; Zhang, S.B. *Phys. Rev. B* **2012**, 86, 121201(R).

[60] H.J. Monkhorst and J.D. Pack, *Phys. Rev. B* **1976**, 13, 5188.

[61] Zhang, S.; Northrup, J. *Phys. Rev. Lett.* **1991**, *67*, 2339–2342.

Figures

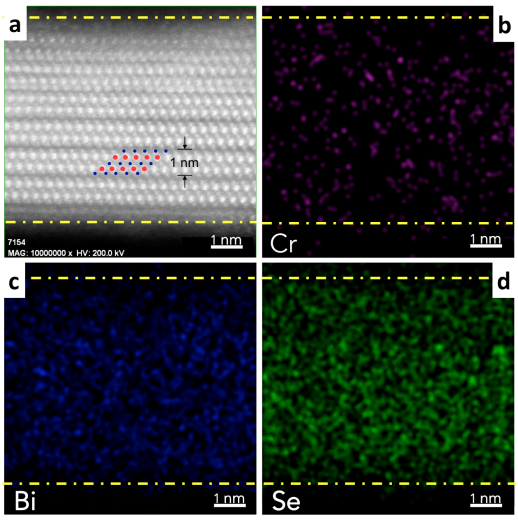

Figure 1. STEM characterization. (a) Typical HAADF image showing the highly ordered hexagonal and quintuple layer structure of the prepared $Bi_{2-x}Cr_xSe_3$/Si(111) thin film samples. The red and blue dots represent the Bi and Se columns, respectively, within one quintuple layer. The dash-dotted lines indicate the boundaries of the $Bi_{2-x}Cr_xSe_3$ thin film with the Al_2O_3 cap and the Si substrate, respectively. (b)-(d) The EDX color maps of (b) Cr, (c) Bi, and (d) As.

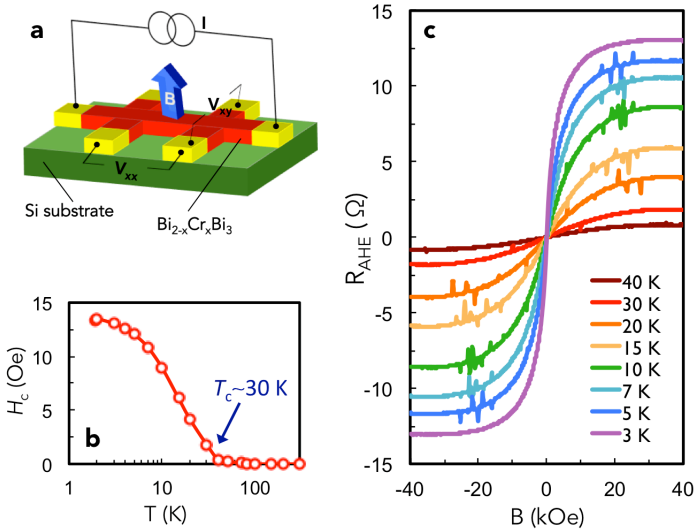

Figure 2. Electrical magneto-transport measurements. (a) Schematic diagram of the experimental setup of the QAH effect measurement. (b) H_c versus temperature of the $Bi_{1.94}Cr_{0.06}Se_3$/Si(111) thin film from 3 to 300 K. (c) R_{AHE} versus magnetic field B of the thin film from 3 to 40 K after background removal.

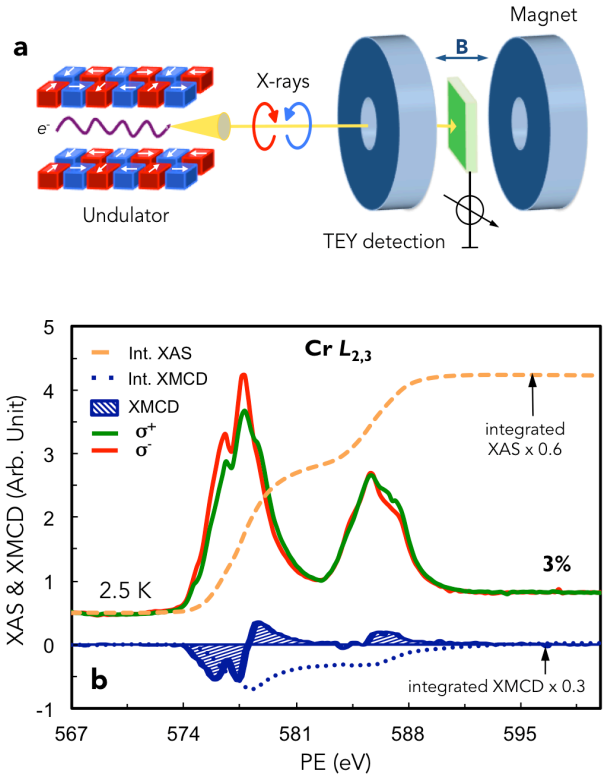

Figure 3. XAS/XMCD measurements. (a) Schematic diagram of the experimental setup for XAS and XMCD at the beamline, where the beamline optics has been omitted. (b) Typical pair of XAS and XMCD spectra of the $Bi_{1.94}Cr_{0.06}Se_3$/Si(111) thin film. Data are offset and scaled for clarity.

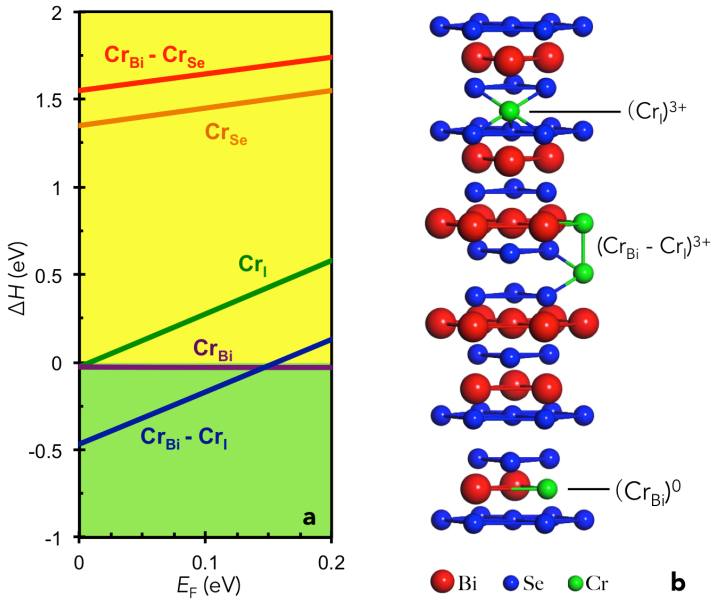

Figure 4. The Cr-related defects in $Bi_{2-x}Cr_xSe_3$. (a) Formation energy ΔH of the Cr-related defects in $Bi_{2-x}Cr_xSe_3$ obtained under the given growth conditions as described in the text. The slopes indicate the stable charge states of the defect, and the zero of E_F corresponds to the valence band maximum (VBM). (b) Illustration of the three types of predominant defects in $Bi_{2-x}Cr_xSe_3$, i.e., Cr_{Bi}^{0}, Cr_I^{3+}, and $(Cr_{Bi} - Cr_I)^{3+}$.

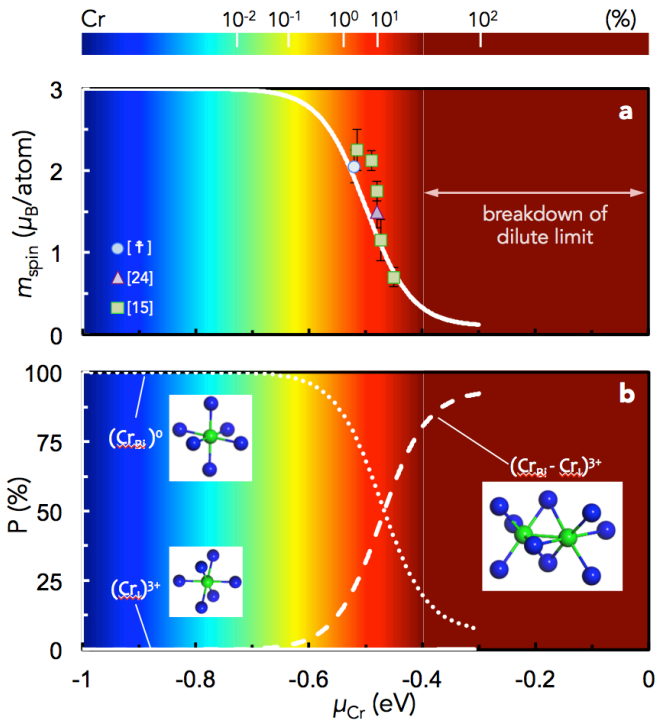

Figure 5. The dependence of (a) m_{spin} and (b) the fraction of the three predominant defects Cr_I^{3+}, Cr_{Bi}^{0}, and $(Cr_{Bi}\text{-}Cr_I)^{3+}$, as a function of the chemical potential of Cr (μ_{Cr}). The zero point of the μ_{Cr} is that of bulk Cr and μ_{Bi} is 150 meV below that of μ_{Bi}^{bulk}. The uppermost scale is an indication of the Cr doping concentration as defined in the text. The brown coloring corresponds to very high defect concentration, in and near where the dilute approximation dramatically fails. The experimentally measured m_{spin} of $Bi_{2-x}Cr_xSe_3$ with varing x have been taken from the literature and gathered in (a) in comparison with the calculation. [†] refers to this work. Note our definition of the doping concentration differs by a factor of ~2.5 that by Hazzen *et al.*, hence the numbers quoted here are larger than that presented in the original paper.[15]